International Journal of Fatigue 192 (2025) 108716

Contents lists available at ScienceDirect

International Journal of Fatigue

journal homepage: www.elsevier.com/locate/ijfatigue

Application of the Effective critical plane approach for the fatigue assessment of ductile cast iron under multiaxial and non-proportional loading conditions

A. Chiocca [a,*], M. Pedranz [b], F. Zanini [c], S. Carmignato [c], V. Fontanari [b], M. Benedetti [b], F. Frendo [a]

[a] Department of Civil and Industrial Engineering, University of Pisa, Pisa, Italy
[b] Department of Industrial Engineering, University of Trento, Trento, Italy
[c] Department of Management and Engineering, University of Padua, Vicenza, Italy

ARTICLE INFO

Keywords:
Effective Critical Plane approach
Multiaxial fatigue
Control volume
Notched component
Ductile cast iron
Non-proportional loading

ABSTRACT

The fatigue assessment of structural components, especially made of ductile cast iron subjected to complex loading conditions, heavily relies on analyzing fatigue damage resulting from stress concentrations induced by geometric irregularities like notches and shrinkage pores. Standard methodologies, encompassing the Theory of Critical Distances (TCD), Strain Energy Density (SED), and Critical Plane (CP), have played pivotal roles in predicting fatigue strength for components featuring such irregularities. In this work, the authors explore the applicability of the Effective Critical Plane (ECP) approach on ductile cast iron notched specimens subjected to multiaxial and non-proportional loading conditions. The method focuses on evaluating the critical plane factor, after averaging the stress and strain field within a given control volume or area (i.e. defined by a control radius), centered on the critical node. The study aims to enhance the accuracy of fatigue life prediction for structural components made of ductile cast iron, thereby contributing to the improvement and practical applicability of fatigue assessment under complex loading conditions. The methodology, integrating the *Smith-Watson-Topper* and *Fatemi-Socie* CP factor, was applied to several experimental fatigue data obtained from ductile cast iron notched specimens, tested under multiaxial non-proportional loading conditions. After establishing the control radius associated with the investigated material, the method was utilized to perform a fatigue life forecast analysis on a specimen with porous defects.

1. Introduction

With the expansion of the energy industry, the importance of ductile cast iron (DCI) is continuously increasing. The peculiar properties of this ferrous alloy, such as the low melting point and the good fluidity, which leads to good castability, allow manufacturers to design and produce complex and large components [1]. Some examples are specific parts of windmills, containers for nuclear waste storage, components for the cement production and bench presses. Long solidification times, associated to the large dimensions of components, can lead to casting defects, such as micro-shrinkage porosity, which can influence the mechanical response of the material. Moreover, these components are generally subjected to multiaxial and time-varying loading, leading to the requirement of suitable multiaxial fatigue criteria, thus allowing for a safe design.

Designing against multiaxial fatigue was initially approached by means of empirical approaches, developed by fitting experimental data. Among these, the most famous are the Gough-Pollard, the Froustey-Lasserre and the Lee formulae [2]. Despite the effectiveness of such approaches to design specific components and geometries, their limitation is their purely empirical nature. They are, indeed, strongly affected by the testing conditions and the tested geometries, limiting their applicability to the stress states and geometries that were actually investigated. For this reason, researchers mainly focused on theoretical approaches, generally applicable to any geometry and loading condition. When developing multiaxial fatigue criteria, several experimental observations should be taken into account. Papadopoulos et. al [2] and Sines et al. [3] reported a little mean shear stress effect on the high-cycle fatigue strength. This effect seems to become stronger while moving

---

[*] Corresponding author.
E-mail address: andrea.chiocca@unipi.it (A. Chiocca).

https://doi.org/10.1016/j.ijfatigue.2024.108716
Received 14 September 2024; Received in revised form 23 October 2024; Accepted 15 November 2024

Nomenclature

$\widehat{\sigma}_{a,i}, \widehat{\tau}_{a,i}$	Stress and shear stress estimators of data points in the experimental fatigue curves
$\widetilde{\mathrm{FS}}$	Effective *Fatemi-Socie* critical plane factor
$\mathrm{P}_{X\%}$	Survival probability rate of X%
$\widetilde{\mathrm{SWT}}$	Effective *Smith-Watson-Topper* critical plane factor
$\mathrm{T}_{\mathrm{ECP}}$	ECP fatigue scatter
E_N	Fatigue prediction error
$N_{f,e}$	Expected number of cycles to failure
N_f	Experimental number of cycles to failure
k_1, k_2, k_3	Fitting parameters of the experimental fatigue curves
$\boldsymbol{x_i}$	Coordinates of the generic nodes i
σ	Standard deviation
$\overline{\sigma}, \overline{\boldsymbol{\varepsilon}}$	Averaged stress and strain tensor
σ_{n}	Maximum normal stress encountered during the load cycle on the selected plane
σ_a, τ_a	Normal and shear stress amplitude
$\sigma_{a,i}, \tau_{a,i}$	Stress and shear stress of the experimental data points
$\sigma_i, \boldsymbol{\varepsilon}_i$	Stress and strain tensor on node i
σ_y	Material's yield strength
E	Young's modulus
G	Shear modulus
IND(•)	Function that yields 1 if the condition within parentheses holds true and 0 otherwise
$\boldsymbol{\varepsilon}_{\mathbf{tot}}$	Strain at failure
λ	Multiaxiality ratio
μ	Mean value
ν	Poisson's ratio
φ	Phase angle between the axial and torsional loadings
N	Number of nodes within the spherical volume or circular area
S	Standard deviation
k	*Fatemi-Socie* material parameter
n	Number of experimental data points used in the regression
p	Number of fitting parameters used in the regression
rc	Control radius
$\Delta\gamma_{\max}$	Maximum shear strain range
$\Delta\varepsilon_{\max}$	Maximum normal strain range
CP	Critical Plane
DCI	Ductile Cast Iron
ECP	Effective Critical Plane
FS	*Fatemi-Socie* critical plane factor
HB	Brinell Hardness
LC	Longest Chord
LP	Longest Projection
MCC	Minimum Circumscribed Circle
NSA	Notch Stress Approach
PDF	Probability Density Function
SED	Strain Energy Density
SWT	*Smith-Watson-Topper* critical plane factor
TCD	Theory of Critical Distances
UTS	Ultimate tensile strength

towards shorter fatigue lives. However, after analyzing the data reported in [4–11], it is clear that the effect of mean shear stresses cannot be ignored when designing against torsional or multiaxial fatigue. Another important experimental evidence regards the fracture morphology of specimens under torsion or multiaxial loading. Berto et. al [11] reported the peculiar "factory roof" morphology in notched steel specimens tested under torsional loading, which leads to rubbing and abrasion, with corresponding energy dissipation. Tanaka [12] confirmed this experimental evidence, showing how the Mode III notch-strengthening effect was due to a cyclic crack surface contact, which explains the abrasion and the formation of debris. Moreover, it was observed that a superposition of torsional cyclic loading and static tension led to a notch-weaking effect, due to the reduction of crack surface contact. The "factory roof" morphology was observed also in notched specimens tested under multiaxial fatigue [11,13], with slightly changing morphology, depending on the phase angle (angle between the cyclic synchronous axial and torsional loadings). Non-proportional out-of-phase loading also influences the experimentally measured fatigue strength. Benedetti et. al [13], Berto et al. [14] and Tovo et al. [8] observed a strengthening effect due to out-of-phase loading in both plain and notched specimens made of DCI. Instead, out-of-phase loading, apparently, has a weakening effect on specimens made of steel [11].

Among the multiaxial fatigue criteria present in the literature, Critical Plane (CP) approaches are the most widespread. Critical plane approaches can generally be regarded as strain-based, stress-based or strain/stress-based, depending on their specific definition. The multiaxial fatigue assessment is performed on a "critical" plane where a certain stress component, strain component, or a combination of both stress and strain components displays its maximum value [15–17]. Furthermore, the critical plane is expected to be the one where fatigue crack nucleates, thus allowing designers to predict the crack nucleation direction. The concept of critical plane was introduced for the first time by Stanfield [18] and then developed by many other authors, like Findley [16], Brown and Miller [19], Kandile [20], Matake [17], Robert [21], and McDiarmid [22,23]. Different stress and strain components were used as fatigue damage parameter: Findley [16] proposed to use the maximum value of a combination of the normal and shear stresses, Brown, Miller and Wang [19,24] the maximum shear strain, Fatemi and Socie (FS) [25] the maximum shear strain, Li, Ince and Glinka [26–29] the maximum value of a combination of normal and shear strains, and Zhong et al. [30] the maximum normal strain on a specific plane. One of the most famous CP approaches is surely the reinterpretation of the Smith-Watson-Topper (SWT) criterion [31] made by Socie [32], from which several modifications were derived. One of the modifications is used in this work. All these authors developed specific formulae to express the dependence of the fatigue life, in terms of cycles to failure N_f, upon specific stress and strain components evaluated on the critical plane, whose direction is fixed and thus not material dependent. Carpinteri et al. [15] observed that the critical plane orientation depends on the material ductility and proposed a framework to define it as a function of the fully reversed axial and torsional fatigue limits.

All the above-mentioned approaches transform specific stress and strain components, or energies, evaluated at a specific location, into equivalent damage parameters that are then associated with a uniaxial curve [33]. Here, the values derived from linear elastic analysis at a specific point may have limited validity since it does not consider factors such as local geometry, material yielding, the presence of singularities in the elastic solution, stress gradients and the size effect [34–36]. Additionally, at the *meso*-scale, material behavior deviates from that of an elastic continuum due to the presence of grains and grain boundaries, further complicating stress–strain evaluations derived from numerical models. One way to overcome this issue is to evaluate the multiaxial fatigue parameters over a small process volume. The concept of "elementary volume" and "structural support length", over which stress or strain components are averaged, was introduced by Neuber a long time ago [37,38], who proposed the well-known Fictitious Notch Rounding approach. The same concept was used to develop the Theory of Critical Distances (TCD) [13,39–45] and strain energy density (SED)-

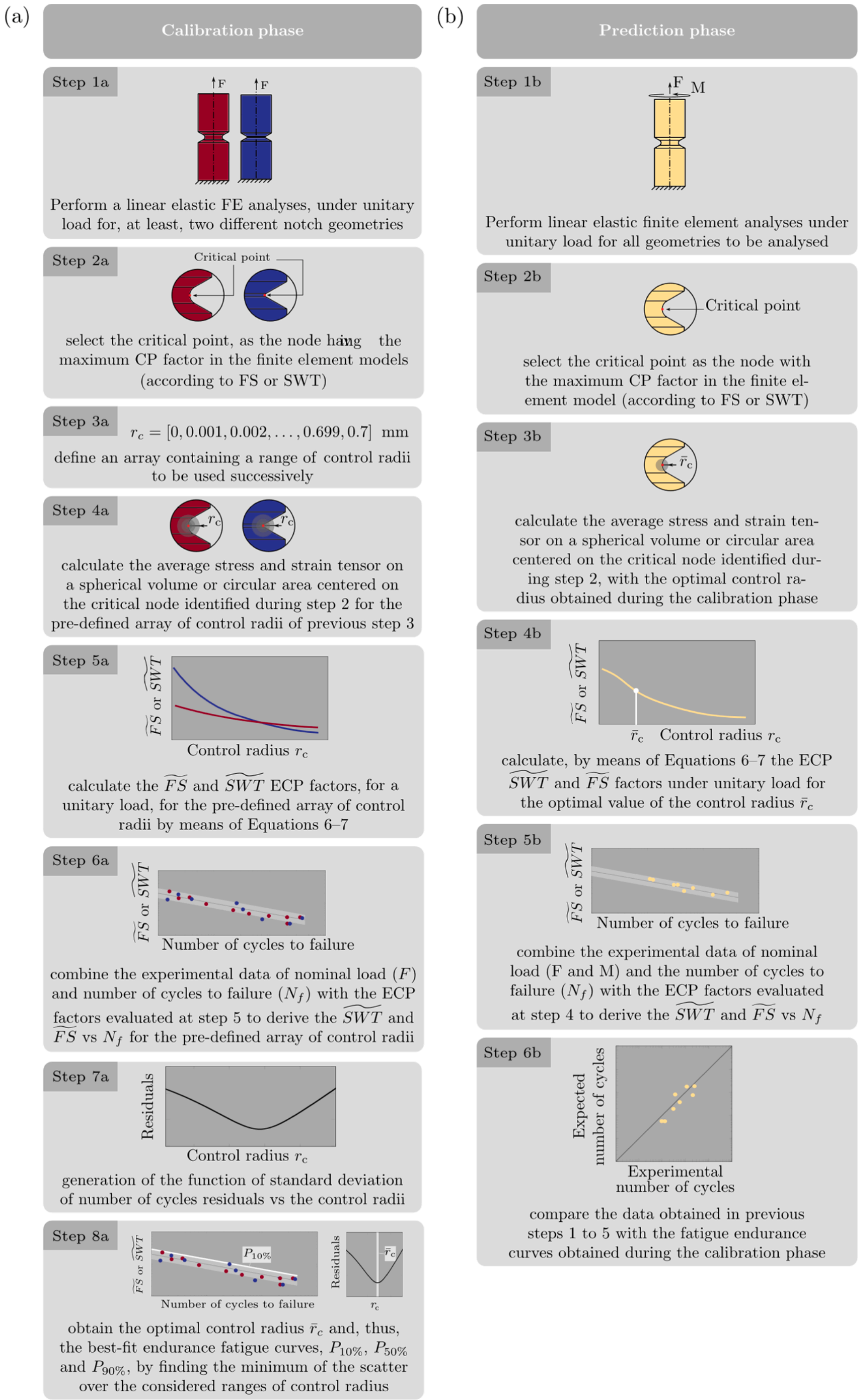

Step 1a Perform a linear elastic FE analyses, under unitary load for, at least, two different notch geometries

Step 2a select the critical point, as the node having the maximum CP factor in the finite element models (according to FS or SWT)

Step 3a $r_c = [0, 0.001, 0.002, \dots, 0.699, 0.7]$ mm
define an array containing a range of control radii to be used successively

Step 4a calculate the average stress and strain tensor on a spherical volume or circular area centered on the critical node identified during step 2 for the pre-defined array of control radii of previous step 3

Step 5a calculate the $\widetilde{FS}$ and $\widetilde{SWT}$ ECP factors, for a unitary load, for the pre-defined array of control radii by means of Equations 6–7

Step 6a combine the experimental data of nominal load (F) and number of cycles to failure (N_f) with the ECP factors evaluated at step 5 to derive the $\widetilde{SWT}$ and $\widetilde{FS}$ vs N_f for the pre-defined array of control radii

Step 7a generation of the function of standard deviation of number of cycles residuals vs the control radii

Step 8a obtain the optimal control radius $\bar{r}_c$ and, thus, the best-fit endurance fatigue curves, $P_{10\%}$, $P_{50\%}$ and $P_{90\%}$, by finding the minimum of the scatter over the considered ranges of control radius

Step 1b Perform linear elastic finite element analyses under unitary load for all geometries to be analysed

Step 2b select the critical point as the node with the maximum CP factor in the finite element model (according to FS or SWT)

Step 3b calculate the average stress and strain tensor on a spherical volume or circular area centered on the critical node identified during step 2, with the optimal control radius obtained during the calibration phase

Step 4b calculate, by means of Equations 6–7 the ECP $\widetilde{SWT}$ and $\widetilde{FS}$ factors under unitary load for the optimal value of the control radius $\bar{r}_c$

Step 5b combine the experimental data of nominal load (F and M) and the number of cycles to failure (N_f) with the ECP factors evaluated at step 4 to derive the $\widetilde{SWT}$ and $\widetilde{FS}$ vs N_f

Step 6b compare the data obtained in previous steps 1 to 5 with the fatigue endurance curves obtained during the calibration phase

Fig. 1. Representation of the method workflow highlighting the method implementation: (a) calibration phase, (b) prediction phase.

based approaches [46–49]. This study makes use of the Effective Critical Plane (ECP) methodology for the fatigue assessment of structural components made of ductile cast iron. Building upon recent advancements in the computational efficiency of critical plane damage parameters, as discussed in prior works by the authors [50–54], the ECP methodology utilizes the underlying averaging concept introduced by Neuber. The ECP, proposed by some of the authors in [55] is based on the common assumption that fatigue cracks are initiated on a small process volume. The proposed method integrates an averaging procedure into the critical plane analysis while maintaining the fundamental insights of the critical plane concept, based on the tensorial description of the stress–strain field, which has been validated by extensive experimental observations. As already discussed in [55], the fact that the CP takes into account the whole stress–strain field appears advantageous, since this allows to deal with complex geometries and loading conditions (e.g. multiaxial non-proportional), after a simple and cost-efficient calibration. Other methods, based on scalar parameter (like SED or NSA) or a combination of different theories (e.g. TCD and SED) sometimes need a longer and more complex, i.e. based on a larger number of parameters, calibration procedure.

The ECP method involves evaluating the averaged stress–strain field within a small volume centered on critical locations, and, afterwards, computing the critical plane factor based on the previously derived averaged tensors. A small sphere is employed in the case of fully three-dimensional geometries, whereas for two-dimensional geometries, a circular area is utilized. The radius of this control region, namely the control radius, is assumed to be material-specific and is determined through a fitting procedure.

To illustrate the method's efficacy compared to existing approaches, the article first provides an explanatory overview of the ECP approach by implementing the two commonly adopted CP parameters, namely *Smith-Watson-Topper* and *Fatemi-Socie* CP factors. Afterwards, experimental fatigue data of ductile cast iron specimens with various notches subjected to different loading conditions are used to investigate the optimal control radius and validate the predictive capability of the proposed methodology in estimating fatigue life. The method capability is validated against specimens with pores as well as without pores, with different notched geometries and subjected to diverse loading conditions.

2. Effective Critical Plane factor

The ECP approach is introduced with reference to the *Smith-Watson-Topper* (SWT) [32] and *Fatemi-Socie* (FS) [25] critical plane factors but can be easily adapted to other CP formulations.

The SWT critical plane factor, incorporating Socie's modification, is expressed in Equation (1):

$$\mathrm{SWT} = \frac{\Delta\varepsilon_{\max}}{2}\sigma_{\mathrm{n}} \tag{1}$$

where, $\frac{\Delta\varepsilon_{\max}}{2}$ represents the amplitude of the maximum normal strain, while σ_{n} denotes the maximum normal stress acting on the plane with the maximum normal strain obtained during the load cycle. The SWT CP factor finds common application in materials susceptible to tensile cracking.

The FS parameter is presented in Equation (2):

$$\mathrm{FS} = \frac{\Delta\gamma_{\max}}{2}\left(1 + k\frac{\sigma_{\mathrm{n}}}{\sigma_y}\right) \tag{2}$$

where, k denotes the material parameter derived through a fitting procedure between uniaxial and torsional data, $\frac{\Delta\gamma_{\max}}{2}$ represents the maximum shear strain amplitude, σ_{n} denotes the maximum normal stress encountered during the load cycle on the plane where the maximum shear strain amplitude is evaluated, and σ_y represents the material's yield strength. This formulation is typically applied for shear-cracking materials, rooted in the maximum shear strain range, in contrast to the SWT model.

2.1. Calibration phase

In order to perform the calibration phase of the ECP method (see Fig. 1a), at least two distinct specimen geometries are required to determine the optimal control radius for the averaging process. The calibration phase involves the spatial averaging of the stress–strain field obtained through linear-elastic finite element analysis under unitary load (Step 1a). In case of specimen controlled geometries, the node j possessing the maximum local CP factor (i.e. SWT or FS in this case) has to be firstly identified (Step 2a):

$$j = \underset{i}{argmax}(\mathrm{CP}_i) \tag{3}$$

This holds for the calibration phase only. For the prediction phase, in general, the critical node has to be determined by an iterative process, as discussed in following section 2.2.

Subsequently, by defining an array of control radii r_c (Step 3a) the volumetric averaged stress and strain tensors (Step 4a) can be determined as follows:

$$\overline{\sigma} = \frac{\sum_i \sigma_i \mathrm{IND}\left(|\boldsymbol{x_i} - \boldsymbol{x_j}| \le r_{\mathrm{c}}\right)}{N} \tag{4}$$

$$\overline{\boldsymbol{\varepsilon}} = \frac{\sum_i \boldsymbol{\varepsilon}_i \mathrm{IND}\left(|\boldsymbol{x_i} - \boldsymbol{x_j}| \le r_{\mathrm{c}}\right)}{N} \tag{5}$$

where, $\boldsymbol{x_i}$ and $\boldsymbol{x_j}$ represents the coordinates of the generic nodes i and j, IND(●) denotes a function that yields 1 if the condition within parentheses holds true and 0 otherwise, while N represents the number of nodes within the spherical volume.

After determining the averaged stress and strain tensors, the ECP parameter, denoted as $\widetilde{\mathrm{FS}}$ or $\widetilde{\mathrm{SWT}}$, can be calculated using one of the existing closed-form solutions found in the literature. For example, Chiocca et al. [54,56] developed analytical formulations that apply to cases of linear elasticity and proportional loading. Other methods, including closed-form or semi-analytical approaches [50,51], are designed for more general conditions involving non-proportional loading and material plasticity. Specifically, the algorithm proposed by Chiocca et al. [51] is utilized for computing both SWT and FS in the context of non-proportional loading, as reflected in the experimental data presented in the following. The methodology relies on the principle that precise fatigue life predictions can be made by considering only the linear elastic stress and strain distributions near regions of stress concentration. This assumption simplifies its practical implementation by efficiently managing three-dimensional stress states caused by complex external forces through the superposition principle. Moreover, the method does not require specific orientations, such as the notch bisector in the TCD method, but rather uses an averaged value within a circular volume or area centered on the critical node—identified as the point with the highest critical plane factor. This generalization makes the method highly adaptable for complex geometries, including porous materials.

The parameters $\widetilde{\mathrm{FS}}$ and $\widetilde{\mathrm{SWT}}$ are computed based on the averaged values of stress and strain tensors ($\overline{\sigma}$ and $\overline{\boldsymbol{\varepsilon}}$) over a specific control radius r_c for a specific load combination F (as presented in Equations (6)–(7). It is important to mention that the F encompasses any external load condition acting on the component, which may be in the form of forces or moments or a combination of them.

$$\widetilde{FS} = \frac{\widetilde{\Delta\gamma_{\max}}}{2}F + \frac{k}{2\sigma_y}\widetilde{\Delta\gamma_{\max}}\widetilde{\sigma}_{\mathrm{n}}F^2 \tag{6}$$

$$\widetilde{\mathrm{SWT}} = \frac{\widetilde{\Delta\varepsilon_{\max}}}{2}\widetilde{\sigma}_{\mathrm{n}}F^2 \tag{7}$$

where $\frac{\widetilde{\Delta\gamma_{\max}}}{2}$, $\frac{\widetilde{\Delta\varepsilon_{\max}}}{2}$ and $\widetilde{\sigma}_{\mathrm{n}}$ represent the averaged values of maximum shear strain amplitude, maximum normal strain amplitude and normal stress, respectively.

By evaluating the averaged stress and strain tensors for different r_c values, it is possible to obtain the formulations $\widetilde{\mathrm{FS}}(r_c)$ and $\widetilde{\mathrm{SWT}}(r_c)$ for each specimen geometry (Step 5a). It is worth noting that linear elastic analyses are commonly employed in methodologies such as NSA, TCD, and SED, which rely on effective stress or stress averaging processes.

Subsequently, by merging $\widetilde{\mathrm{FS}}$ and $\widetilde{\mathrm{SWT}}$ with the experimental number of cycles to failure corresponding to different load values (Step 6a), the reference endurance curve can be established, for any value of the control radius defined in the array r_c. The optimal $\overline{r}_c$ along with the resultant design fatigue curve, is then determined through the minimization of the standard deviation of the residuals of the number of cycles (Step 7a). Once the reference endurance curve and control radius are derived, they can be employed for the fatigue assessment of any

Table 1
Chemical composition and mechanical properties of the investigated EN-GJS-600–3 ductile cast iron (data taken from [48]).

C (%)	Si (%)	Mn (%)	P (%)	S (%)	Cu (%)	Ni (%)	Mg (%)
3.55	2.39	0.28	0.038	0.009	0.52	0.02	0.046
E (GPa)	**G (GPa)**	**σ_y (MPa)**	**UTS (MPa)**	**ε_{tot} (%)**	**ν**	**HB**	
174 ± 2	68.5 ± 1.3	363 ± 8	485 ± 15	2.1 ± 0.5	0.27	198 ± 4	

component made of the same material, using the same ECP damage parameter accordingly (Step 8a). It should be noted that at least two experimental fatigue curves derived from specimens with a different degree of notch severity are required for the calibration phase. The curves to be used can be derived from simple tensile fully reversed fatigue tests; indeed, the use of a critical plane factor as an equivalent parameter during the prediction phase is expected to account for the type of loading.

2.2. Prediction phase

At this point the method can be applied for fatigue prediction analyses of components possessing the same material but different geometry and loading conditions (see Fig. 1b). The prediction phase also involves the use of linear elastic finite element simulations under unitary load (Step 1b) and the identification of the node with maximum local CP (Step 2b). Subsequently, stress and strain tensors are averaged over a volume defined by the optimal radius $\bar{r}_c$ (Step 3b) in order to calculate ECP factors (Step 4b). Subsequently, the fatigue life prediction can be performed using the endurance curves evaluated during the calibration phase (Step 5b) to obtain the expected number of cycles to failure (Step 6b). The endurance curve is a designer's choice, and according to the degree of conservatism different curves related to various failure probabilities can be chosen.

It is worth noting that up to this point the node with maximum CP has been considered to be the one providing the maximum ECP value. Typically, this occurs on controllable notch geometries, such as notches produced by machining (e.g. V-notch, U-notch). However, for complex notch geometries, such as micro shrinkage pores, it is not necessarily the case that the node that experiences the highest local CP value should provide the highest ECP value, due to the gradient in the stress field. Therefore, it is highly recommended to employ controlled notch ge-

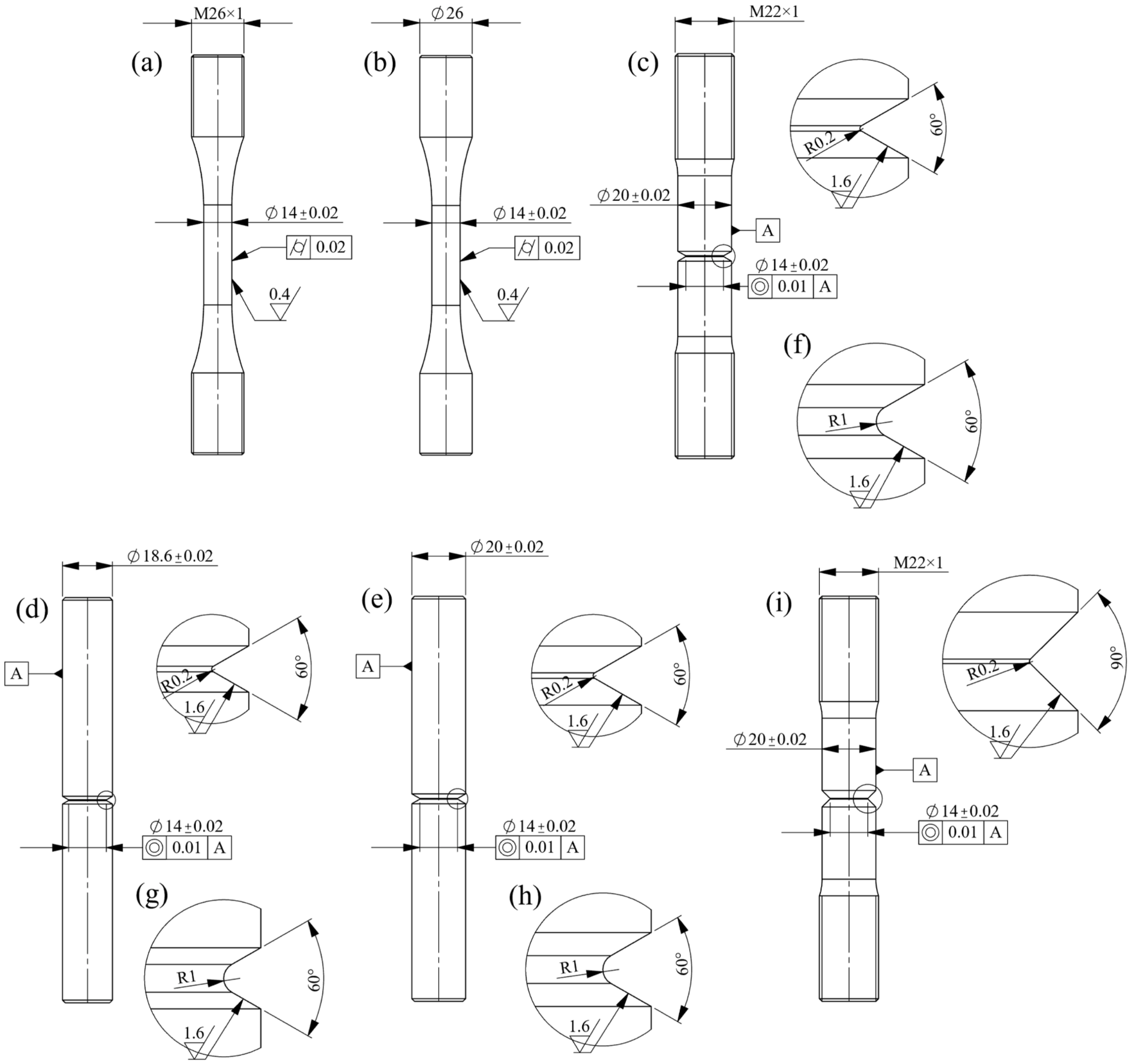

Fig. 2. Geometries of the specimens investigated for uniaxial, torsional and multiaxial fatigue (this picture is a reproduction taken from [48]).

Table 2
Fatigue parameters of the investigated data set taken from [48].

Geometry	Loading conditions	k_1 (MPa)	k_2 (MPa)	k_3	σ_a at 5 × 10^6 cycles (MPa)	S (MPa)
Plain (a)	Axial, R = − 1	123	3304.9	0.288	161.9	10.0
Sharp notch (c)	Axial, R = − 1	79.2	12,062	0.423	96.9	8.4
Sharp notch 90° (i)	Axial R = 0.1	21	723	0.198	55.1	3.6
Blunt notch (f)	Axial, R = − 1	78.2	2980.9	0.280	117.9	8.9
Blunt notch (f)	Axial, R = 0.5	–	461.5	0.150	45.3	1.3
Plain (b)	Torsional, R = − 1	–	899.2	0.112	159.8	9.9
Sharp notch (d)	Torsional, R = − 1	–	470.3	0.065	172.6	24.6
Blunt notch (g)	Torsional, R = − 1	–	593.9	0.073	192.6	4.6
Blunt notch (g)	Torsional, R = 0.1	–	710.1	0.129	97.5	5.7
Plain (b)	λ = 1, R = − 1, φ = 0°	–	761.5	0.138	90.6	7.4
Plain (b)	λ = 1, R = − 1, φ = 90°	–	374.8	0.068	131.3	5.5
Sharp notch (e)	λ = 1, R = − 1, φ = 0°	–	285.2	0.088	73.4	3.6
Sharp notch (e)	λ = 1, R = − 1, φ = 90°	–	421.6	0.098	93.0	3.2
Blunt notch (h)	λ = 1, R = − 1, φ = 0°	–	609.7	0.129	81.7	6.3
Blunt notch (h)	λ = 1, R = − 1, φ = 90°	–	442.7	0.093	104.5	5.5
Blunt notch (h)	λ = 2, R = − 1, φ = 0°	–	544.7	0.157	48.1	2.6
Blunt notch (h)	λ = 2, R = − 1, φ = 45°	–	366.1	0.117	60.6	5.4
Blunt notch (h)	λ = 2, R = 0.1, φ = 45°	–	415.7	0.465	32.5	0.27

ometries for the calibration phase. In contrast, during the prediction phase, Steps 2b, Step 3b, and Step 4b must be iterated, for decreasing CP local values. For each local decreasing CP value, the ECP, obtained at the given $\bar{r}_c$, is calculated and the current maximum ECP parameter is updated. This process is stopped when the currently stored maximum ECP factor is greater than the next obtained local CP factor; in other words, the iteration is running as long as the maximum local CP value (e.g. FS or SWT) is greater than or equal to the currently stored maximum ECP factor.

3. Materials and methods

The experimental data sets used in this work were already published by Pedranz et. al in [48,49] and are here used to validate the proposed ECP approach. The material investigated is a ductile cast iron grade EN-GJS-600–3, characterized by an almost fully pearlitic matrix. The chemical composition and the material's properties are reported in Table 1.

As explained in [48], the tested specimens were extracted from casts characterized by a high thermal modulus (about 6 cm) and a long solidification time, which is representative of large DCI components. In particular, the material was produced by casting cylinders with a diameter of 300 mm and a height of 520 mm, affected by a total solidification time of about 200 min. The specimens were then extracted and machined from the core part of the cylinders, which displayed a homogenous solidification rate.

The experimental axial, torsional and multiaxial fatigue campaign was conducted on plain and notched specimens, whose geometries are shown in Fig. 2.

Specimens (a, c, f, i) were tested under uniaxial fatigue, specimens (b, d, g) were tested under torsional fatigue, and specimens (e, h) were tested under multiaxial fatigue. The actual notch radii of the notched specimens were measured by stereomicroscopy and found to be 0.3 mm for (c), 0.23 mm for (d) and (e), and 1 mm for (f, g, h).

The uniaxial fatigue tests were carried out using a Rumul (Switzerland) Testronic resonant resting machine, at a nominal frequency of 150 Hz. The torsional and multiaxial fatigue tests were carried out using a Walter + Bai (Switzerland) LFV100-T1000-HH biaxial servo-hydraulic machine, equipped with hydraulic grips and a biaxial load cell with axial and torsional load capacities of 100 kN and 1000 Nm, respectively. This machine operated at a frequency comprised between 15 and 20 Hz. The multiaxial fatigue tests were performed at a constant frequency, identical for the axial and torsional loadings, and investigated different combinations of the phase angle between the loading modes, the biaxiality ratio and the stress ratio.

The experimental axial data were fitted by the following asymptotic equation, which represents the 50 % failure probability and is non-linear in a log–log plot, thus capturing the knee observed in the data:

$$\sigma_a = k_1 + \frac{k_2}{N_f^{\,k_3}} \tag{8}$$

The experimental torsional and multiaxial fatigue data were instead fitted by the Basquin law, as the data don't show any knee:

$$\tau_a = \frac{k_2}{N_f^{\,k_3}}; \sigma_a = \frac{k_2}{N_f^{\,k_3}} \tag{9}$$

The scatter band was assessed by calculating the estimated regression variance, which was considered to be constant over the investigated fatigue life range for each data set:

$$S^2 = \frac{\sum_{i=1}^{n}\left(\sigma_{a,i} - \widehat{\sigma}_{a,i}\right)^2}{n-p}; S^2 = \frac{\sum_{i=1}^{n}\left(\tau_{a,i} - \widehat{\tau}_{a,i}\right)^2}{n-p} \tag{10}$$

All the uniaxial, torsional and multiaxial fatigue data analyzed in this work are listed in Appendix A of [48]. The parameters of the fitting equations are listed in Table 2.

As highlighted in [13] and [48], the investigated DCI grade shows a peculiar behavior when tested against fatigue. Firstly, fatigue failures are triggered by different features, depending on the geometry investigated. The fatigue crack is always nucleated by micro shrinkage pores in plain specimens, and it is generally nucleated by graphite nodules at the notch in notched specimens. This experimental evidence is strictly related to the spatial distribution of the micro shrinkage pores and to the probability of finding a pore in the vicinity of a notch. This behavior was modeled by Pedranz et al. in [49] through the concept of highly stressed volume. The highly stressed volume is much smaller in notched specimens compared to plain specimens, thus lowering the probability of finding shrinkage pores close to the notch, where stress intensification appears. If a shrinkage pore lies far enough from the notch, where stresses are much lower, the pore becomes less critical than the notch itself, and fatigue damage is triggered by the geometrical notch. Another important characteristic regards the phase angle between the axial and torsional loads. If out-of-phase loadings are applied, the fatigue life increases, thus creating a beneficial effect on the material. Such different fatigue failure behavior between plain and notched specimens is the reason why the calibration step will be entirely carried out employing notched specimens, thus not encountering dissimilar fracture mechanisms during calibration.

To further extend the validation of the approach proposed in the work, two plain specimens, tested under uniaxial and torsional fatigue, respectively, were accurately analyzed. The specimen denoted as "Plain Axial (a)" was tested under uniaxial fatigue at a stress amplitude of 140

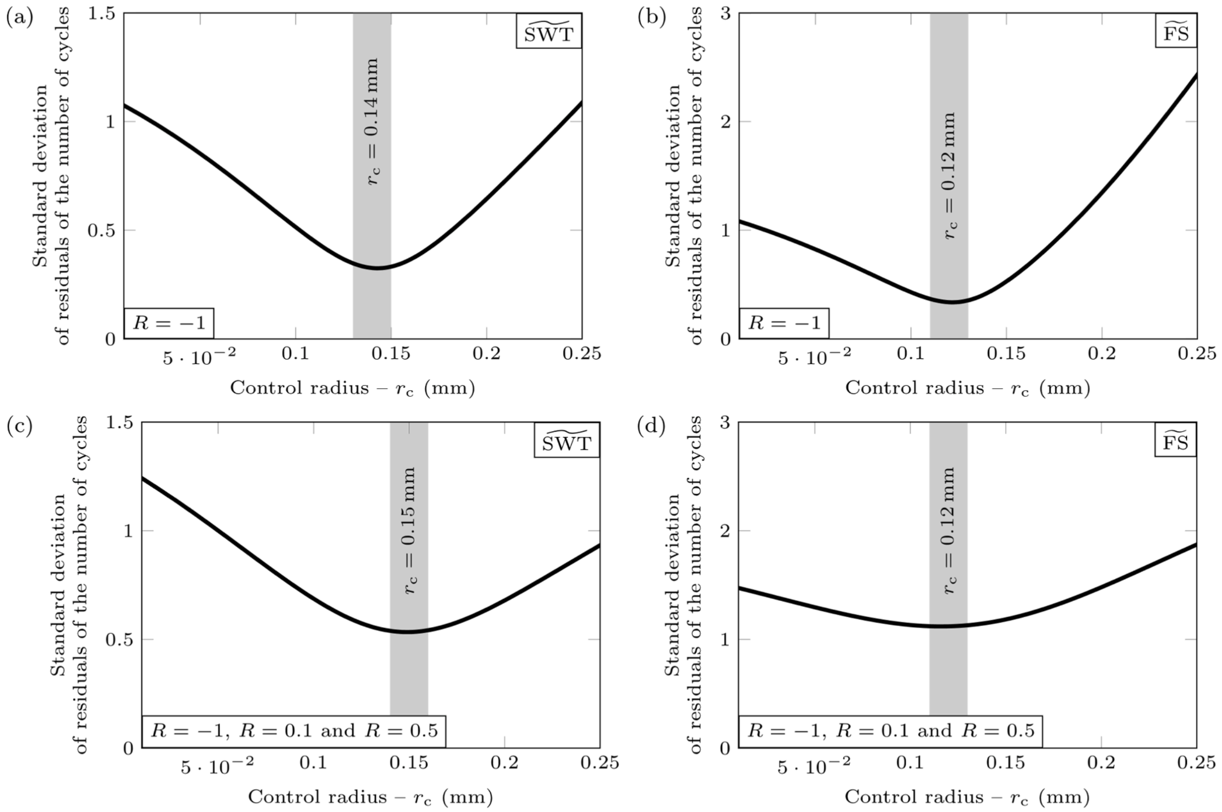

Fig. 3. Standard deviation of residuals of the number of cycles for the Blunt notch and Sharp notch geometries tested under a loading ratio of R = −1 for both the $\widetilde{\text{SWT}}$ model (a) and $\widetilde{\text{FS}}$ model (b), and under loading ratios of R = −1, R = 0.1, and R = 0.5 for the $\widetilde{\text{SWT}}$ model (c) and $\widetilde{\text{FS}}$ model (d).

MPa and load ratio R = −1, failing ad about 2 million cycles. The specimen denoted as "Plain Torsion (b)" was tested under torsional fatigue at a shear stress amplitude of 180 MPa and load ratio of R = −1, failing at 754,196 cycles. Both specimens were analyzed through metrological X-ray computed tomography (CT) with a voxel size of 5.8 µm, using a Nikon Metrology MCT225 system (Nikon Metrology, UK), characterized by micro-focus X-ray source (minimum focal spot size equal to 3 µm), 16-bit flat panel detector with 2000 × 2000 pixel grid, and temperature controlled cabinet (20 ± 0.5 °C). Surfaces of the detected shrinkage pores were determined from 3D CT reconstructions using the local-adaptive algorithm implemented in the elaboration software VGStudio MAX (Volume Graphics GmbH, Germany), meshed and included in 3D models for finite element analyses (see Section 4.3). Specimen "Plain Axial (a)" was already analyzed by Pedranz et al. in [49] adopting a SED-based approach, while specimen "Plain Torsion (b)" is analyzed for the first time in this work.

4. Results and discussion

In this section, the outcomes of the model calibration and fatigue life prediction analysis will be presented and analyzed, both in the case of notched specimens and plain specimens in the presence of internal pores.

4.1. ECP model calibration

To derive the material parameter r_c and the fatigue endurance curve, two specimen geometries under uniaxial tensile loading conditions, namely Blunt notch and Sharp notch in the following, were utilized (i.e. the reference geometries are represented in Fig. 2c-f respectively). In order to check the robustness of the control radius this was determined under varying load ratio conditions, specifically employing axial data solely at R = −1 or incorporating all available axial data at R = −1, R = 0.1, and R = 0.5. The minimization of the standard deviation of the number of cycles residuals over r_c provides the optimal control radius. The residuals were calculated as the difference between the logarithms of experimental cycle to failure and their expected values (i.e. determined by means of the $P_{50\%}$ curve) and serve as an indicator of the fatigue scatter derived from the reference data. By selecting the minimum of the standard deviation of residuals function, the optimal size of the control volume is obtained, effectively capturing diverse geometric notch severities, i.e., Blunt notch (f) and Sharp notch (c). It is worth noting that minimizing the standard deviation of the residuals allows calibration to be performed with more than two experimental curves.

The results are represented in Fig. 3, illustrating the standard deviation of the residuals over the control radius Fig. 3a-b showcase the results for axial data solely under R = −1 for the $\widetilde{\text{SWT}}$ and $\widetilde{\text{FS}}$ models, while Fig. 3c-d presents the analysis of axial data across all available load ratios for the $\widetilde{\text{SWT}}$ and $\widetilde{\text{FS}}$ models. Notably, employing a larger dataset of experimental data (i.e., at different load ratios) insignificantly influences the optimal control radius value, standing at $r_c = 0.14$ mm for $\widetilde{\text{SWT}}$ and $r_c = 0.12$ mm for $\widetilde{\text{FS}}$. This result indicates how the ECP method inherently accommodates mean stress variation due to the σ_n parameter embedded in both SWT and FS formulations. For this reason, only the calibration parameters (i.e. control radius and design curve) derived from analysing the experimental dataset at R = −1 will be employed for subsequent predictive analyses.

Another important aspect of the calibration phase concerns the derivation of the design curve. Fig. 4 illustrates the calibration curves obtained for the $\widetilde{\text{SWT}}$ and $\widetilde{\text{FS}}$ models, each calibrated with distinct control radii set at at $r_c = 0.14$ mm and $r_c = 0.12$ mm, respectively. These calibration curves are presented based on selected survival probability rates, specifically $P_{10\%}$, $P_{50\%}$ and $P_{90\%}$. The resulting curves exhibit minimal dispersion characterized by fatigue scatter of $T_{ECP} = 1 : 1.25$ for $\widetilde{\text{SWT}}$ and $T_{ECP} = 1 : 1.17$ for $\widetilde{\text{FS}}$.

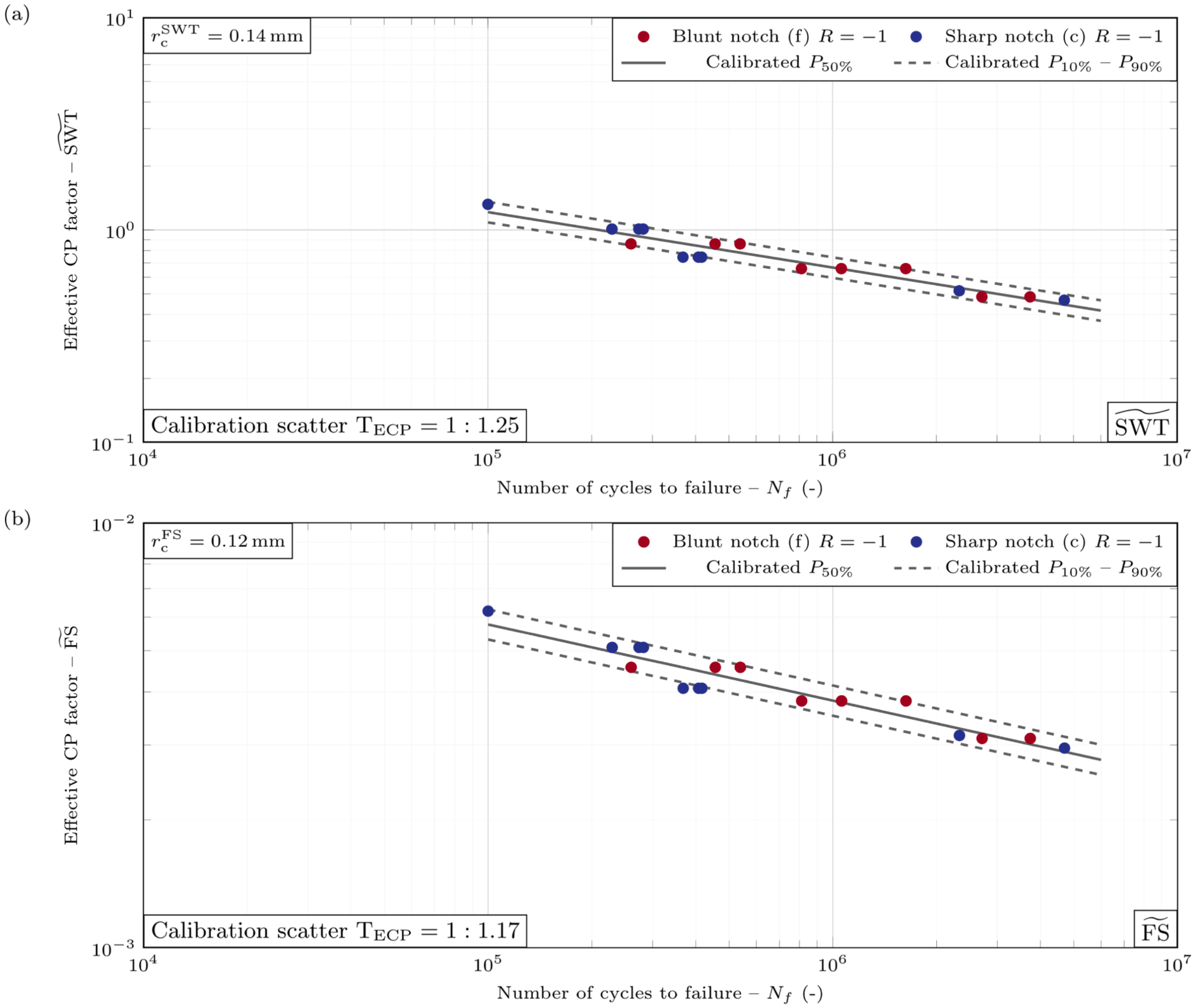

Fig. 4. Endurance curves calibrated using experimental data from tensile fatigue tests as reported in [48], with a control radius of $r_c = 0.14mm$ for the $\widetilde{\text{SWT}}$ model (a) and of $r_c = 0.12mm$ for the $\widetilde{\text{FS}}$ model (b).

After obtaining the optimal control radius and the design curves, it is possible to analyze other notch geometries subjected to different loading conditions. The remaining geometries presented in Section 3 were investigated using the $\widetilde{\text{SWT}}$ and $\widetilde{\text{FS}}$ models, and the results are presented in Fig. 5 and Fig. 6.

Fig. 5 presents $\widetilde{\text{SWT}}$ and $\widetilde{\text{FS}}$ models' implementation for all analyzed cases of Section 3 except for the data used for calibration, along with the previously obtained design curves. It can be noted that a greater dispersion around the design curves $P_{10\%}$, $P_{50\%}$ and $P_{90\%}$ is present in the case of the $\widetilde{\text{FS}}$ method compared to the $\widetilde{\text{SWT}}$ method. This is further highlighted by the results presented in Fig. 6, which compare the number of experimental and expected number of cycles to failure for all geometries and loading conditions investigated. Along with the experimental points, fatigue scatter bands for factors 2, 3, and 5 are provided. Considering the entire available set of experimental data, most of the points fall within the fatigue scatter band of factor 3 when considering the $\widetilde{\text{SWT}}$ model, whereas most of the data falls outside the scatter band of factor 3 when implementing $\widetilde{\text{FS}}$.

To evaluate the effectiveness of the proposed ECP method the error in fatigue assessment was calculated using the parameter employed by Walat et al. [57] and presented in Equation (11):

$$E_N = log\left(\frac{N_f}{N_{f,e}}\right) \tag{11}$$

where N_f and $N_{f,e}$ represent the experimental and expected fatigue lives, respectively. Fig. 7 shows the Probability Density Function (PDF) of E_N (i.e. assuming a normal distribution) employing different calibration datasets, namely the calibration with the axial loaded specimen at R = -1 and the axial loaded specimen under R = -1, R = 0.1, and R = 0.5 along with the distributions obtained from the implementation of the classic definition of FS and SWT critical plane factors. It is evident how the implementation of $\widetilde{\text{SWT}}$ leads to a much more contained mean value and standard deviation compared to the $\widetilde{\text{FS}}$ model. The mean value (μ) and standard deviation (σ) vary slightly as the loading ratio varies in the case of $\widetilde{\text{SWT}}$ and $\widetilde{\text{FS}}$. The implementation of standard critical plane methods does increase significantly the dispersion, the primary cause is certainly related to the application of FS and SWT to notched specimens under linear-elastic material hypothesis. Although the application of CP factors under linear elastic material conditions may not have much practical sense, nevertheless, these results can provide the reader with a broader insight into the improvement obtained by applying the ECP method, while being aware that ECP and CP are hardly comparable in the context of linear elasticity.

The superior performance of $\widetilde{\text{SWT}}$ over $\widetilde{\text{FS}}$ can be attributed to the brittle behavior of the investigated material, which is better described by a tensile-based formulation like SWT compared to a shear-based formulation derived from FS. Similar results were obtained by Kraft

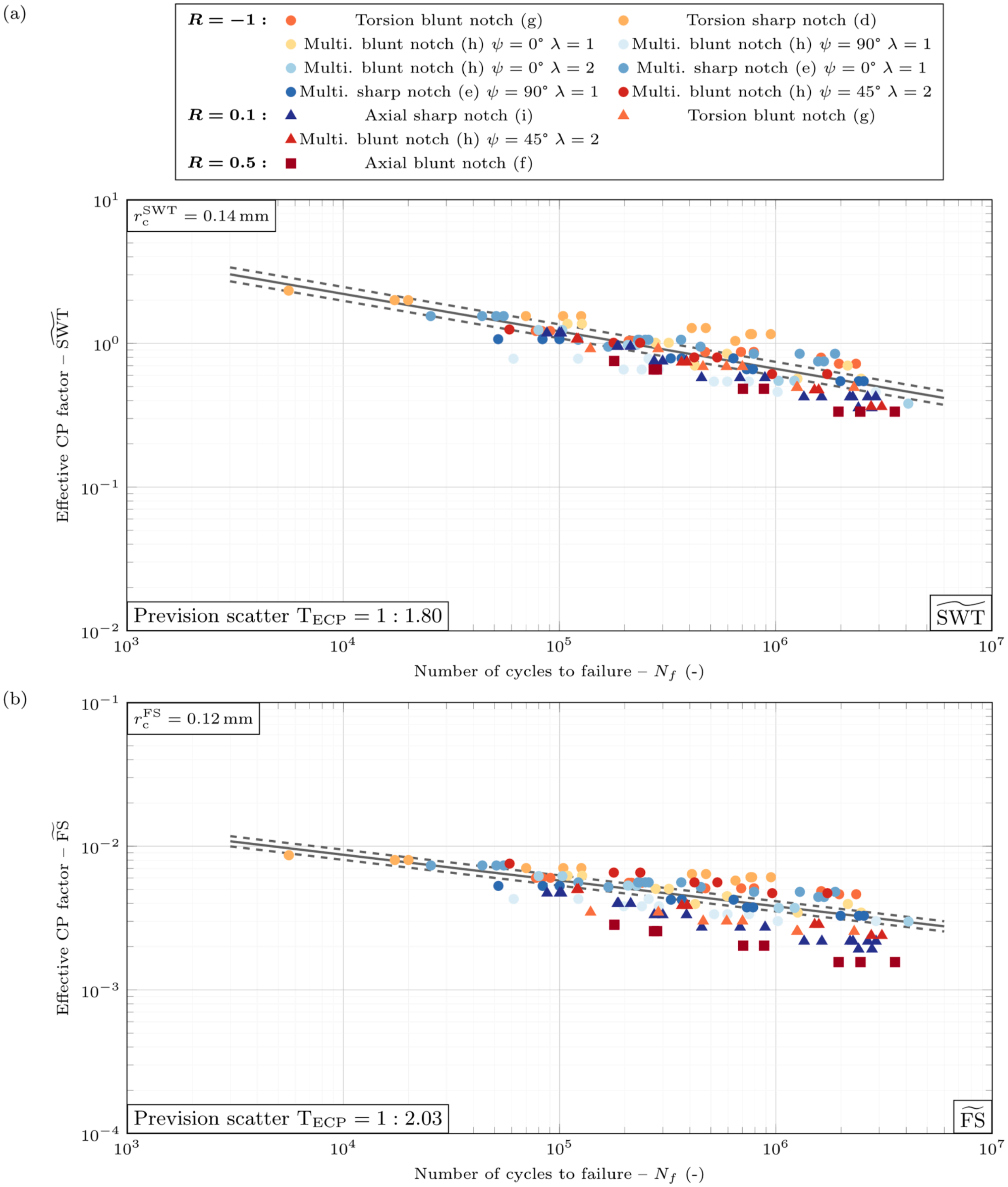

Fig. 5. Comparison of Effective Critical Plane factors $\widetilde{\mathrm{SWT}}$ against the number of cycles to failure (a) and $\widetilde{\mathrm{FS}}$ against the number of cycles to failure (b) for various notched geometries, based on data from [48]. The fatigue data include uniaxial and multiaxial in-phase and out-of-phase loading conditions, along with the calibrated endurance curves $P_{10\%}$, $P_{50\%}$ and $P_{90\%}$ of Fig. 4.

et al. [58], applying SWT and FS on plain specimens tested under non-proportional fatigue loading for a GJS-500 cast iron. Concerning multiaxial data analysis, it is important to note that the determination of $\Delta\gamma_{max}$, essential for establishing the $\widetilde{\mathrm{FS}}$ factor, has been conducted through the Minimum Circumscribed Circle (MCC) technique. It is worth noting that the MCC method, along with other methods like the Longest Chord (LC) and Longest Projection (LP), faces limitations in accurately distinguishing between proportional and non-proportional loading paths. However, it was deemed unnecessary to investigate more advanced methods since the data providing the highest error relative to the design curves are purely axial data (see Fig. 5), for which the aforementioned methods do not differ in terms of $\Delta\gamma_{max}$ evaluation.

4.2. *ECP model prediction on plain porous specimens*

The calibrated ECP model was further applied to specimens of nominal plain geometry (see Fig. 2a-b and Fig. 8). In contrast to the previous cases of notch specimens, as shown in [48], in the absence of

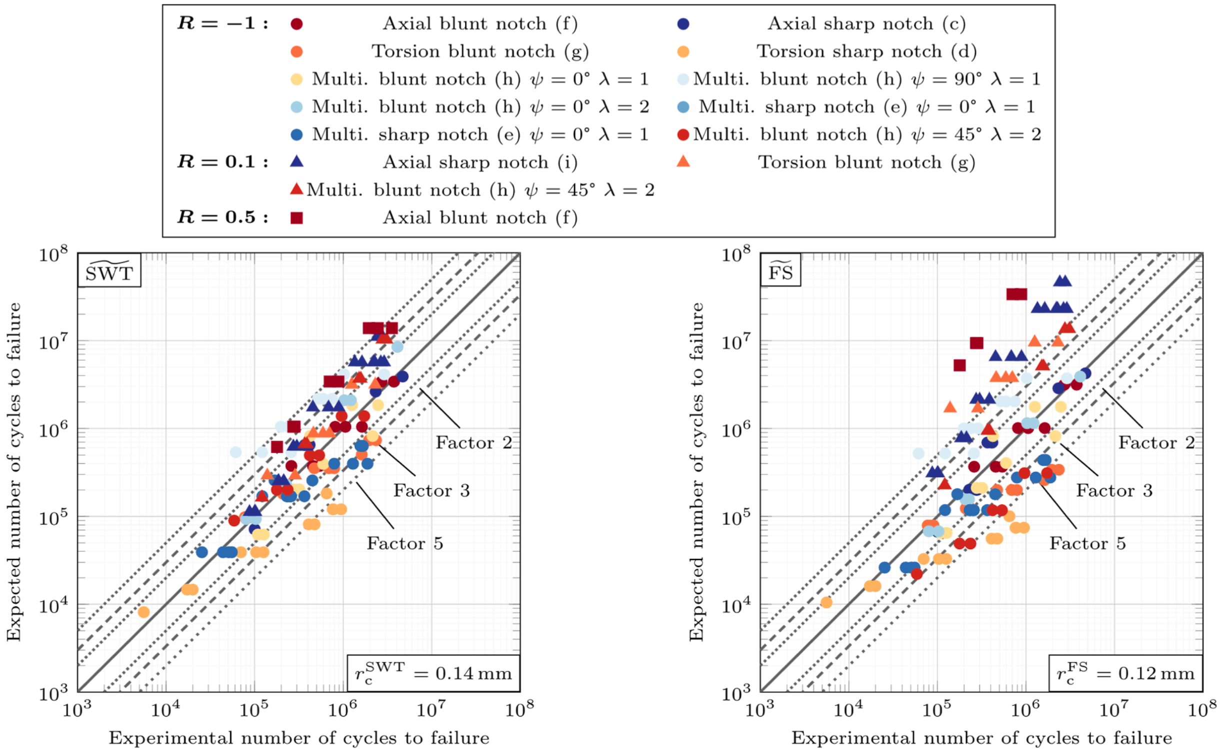

Fig. 6. Comparison between expected and experimental fatigue life for various notched geometries and loading conditions, using the $\widetilde{\mathrm{SWT}}$ and $\widetilde{\mathrm{FS}}$ critical plane factors, based on data from [48].

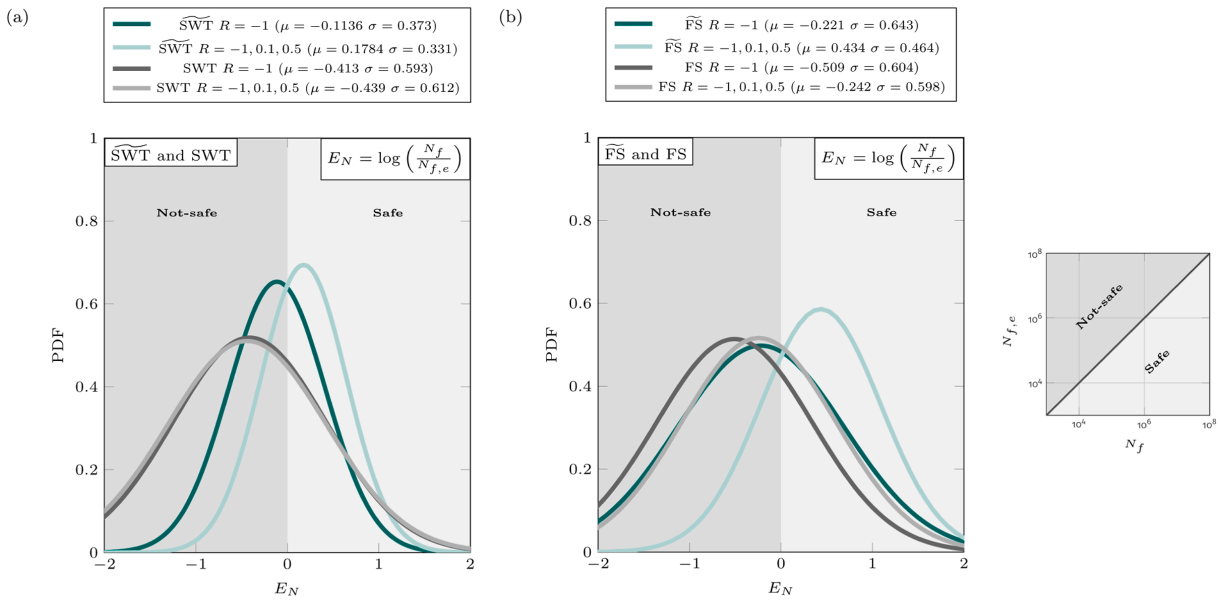

Fig. 7. Probability density function in the case of a normal distribution of $\mathrm{E_N}$, for $\widetilde{\mathrm{SWT}}$ and SWT (a) and for $\widetilde{\mathrm{FS}}$ and FS (b).

intentionally introduced notches, the pore results as the critical fatigue defect and must therefore be taken into account for the application of the ECP method. It is worth noting that the pores resulting to be critical (and presented in Fig. 8) exhibit non-negligible size when compared to the specimen dimensions. They exhibit a maximum Feret diameter, computed in a plane perpendicular to the specimen axis, equal to 2300 μm and 3900 μm, respectively for the “Plain Axial (a)” and “Plain Torsion (b)” specimens.

Finite element simulations of the pore models were post-processed using the ECP $\widetilde{\mathrm{SWT}}$ and $\widetilde{\mathrm{FS}}$ approaches. In the case of pore geometries, the critical values of $\widetilde{\mathrm{SWT}}$ and $\widetilde{\mathrm{FS}}$ were found in the case of a control volume not centered on the node having the local maximum CP factor of FS and SWT, respectively. It was necessary to iterate the ECP algorithm (Step 2b, Step 3b, and Step 4b of Fig. 1) by searching for nodes with decreasing FS and SWT values until the maximum ECP was identified with respect to the calibrated $r_c{}^{SWT}$ and $r_c{}^{FS}$. The algorithm was arrested when the local maximum CP value (i.e. FS and SWT) was less than or equal to the maximum calculated ECP factor (i.e. evaluated for a specific control radius) as previously described in section 2.2.

Equations (12), (13) outlines the algorithm’s arresting criterion,

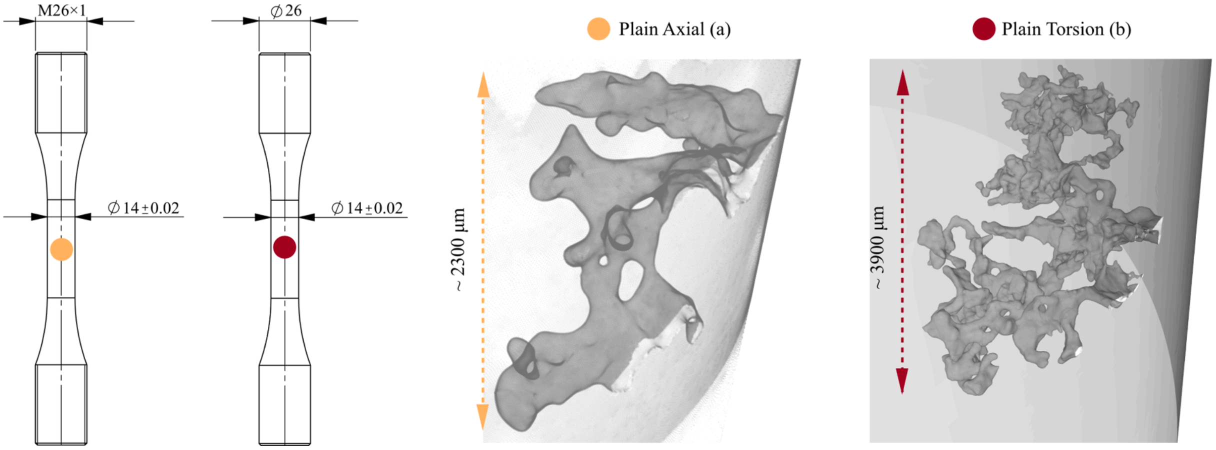

Fig. 8. Plain specimen geometries and pore geometries obtained by CT scan and modeled through finite element analysis. The tensile specimen model is taken from [49].

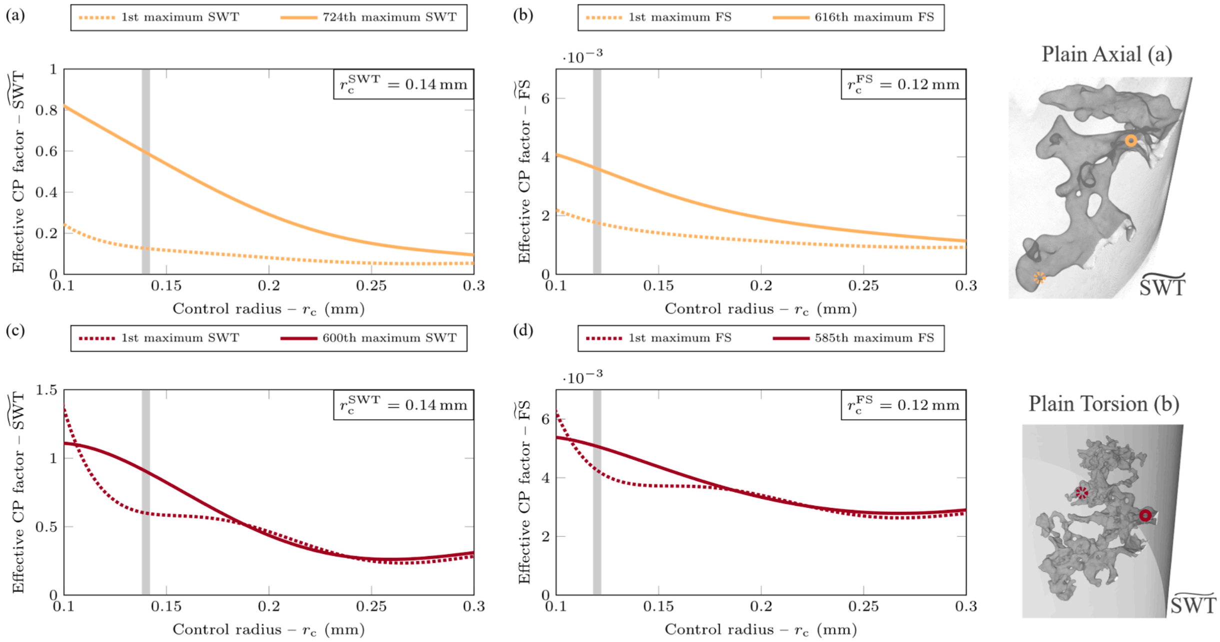

Fig. 9. Effective CP factor vs control radius for different nodal location with decreasing local CP maximum for the “Plain Axial (a)” and “Plain Torsion (b)” specimens: $\widetilde{SWT}$ vs r_c for the specimen under tensile loading (a), $\widetilde{FS}$ vs r_c for the specimen under tensile loading (b), $\widetilde{SWT}$ vs r_c for the specimen under torsion loading (c) and $\widetilde{FS}$ vs r_c for the specimen under torsion loading (d). The tensile specimen model is taken from [49]. It has to be noted that all the plots start from $r_c = 0.1mm$ and that for $r_c = 0mm$ the dashed curve gives greater CP factor than the solid line; this can be appreciated in plots (c) and (d).

where i represents the node with the maximum local CP factor, while j represents the next node, in a decreasing order of local CP value:

$$SWT_j \leq max\left(\widetilde{SWT}_k\left(r_c{}^{SWT}\right)\right) \text{ for } k = i, \cdots, j \tag{12}$$

$$FS_j \leq max\left(\widetilde{FS}_k\left(r_c{}^{FS}\right)\right) \text{ for } k = i, \cdots, j \tag{13}$$

Fig. 9a-b display the $\widetilde{SWT}$ vs r_c and $\widetilde{FS}$ vs r_c curves with respect to a volume centered on the node exhibiting the first CP maximum as well as on the node yielding the maximum ECP value for the “Plain Axial (a)” specimen (i.e. subjected to pure tensile load). Similarly, Fig. 9c-d provide the same comparison for the “Plain Torsion (b)” specimen (i.e. subjected to pure torsional load). In both scenarios, a significant difference in ECP values can be noticed depending on the control volume’s reference position. Such a result provides evidence how, for very complex geometries, the maximum value of the ECP parameter (i.e., derived from tensor averaging applied to the critical plane methodology) is not necessarily located over the point achieving a local CP maximum. Algorithms for speeding up the calculation of the critical plane factors are crucial in this context since SWT and FS had to be calculated for all nodes belonging to pore geometries. In this scenario, more than 240,000 nodes were required to be analyzed for each pore model by using the finite element method, which required approximately three minutes via the use of optimized counting methods already presented by some of the authors [50,51,54,56].

The ECP method, by means of the averaging procedure, considers a process volume thus avoiding solutions linked to geometric singularities or high stress-state gradients caused by the assumption of linear elasticity.

It should be noted that since the method is based on volumetric averaging of stress and strain tensors, it requires that there must always

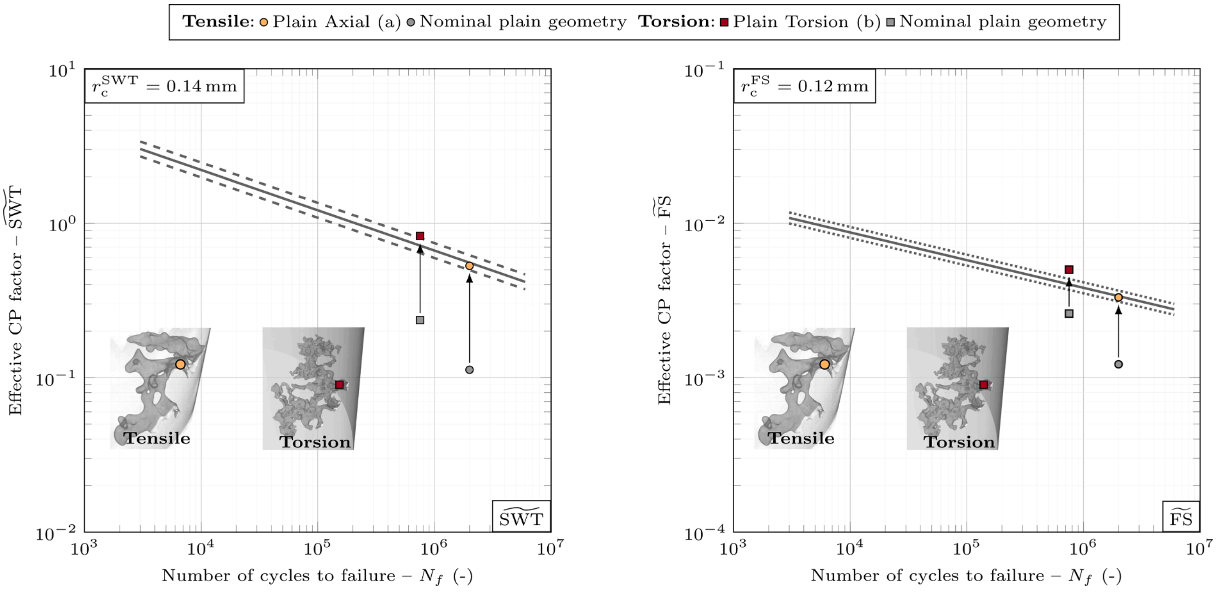

Fig. 10. Effective CP factors $\widetilde{\text{SWT}}$ vs number of cycles to failure and $\widetilde{\text{FS}}$ vs number of cycles to failure for porous plain specimens under fully reversed tensile and torsion loading conditions, together with the calibrated endurance curves $P_{10\%}$, $P_{50\%}$ and $P_{90\%}$. The geometry of actual pores extracted from 3D CT reconstructions was included in the plain specimen. The tensile specimen model is taken from [49].

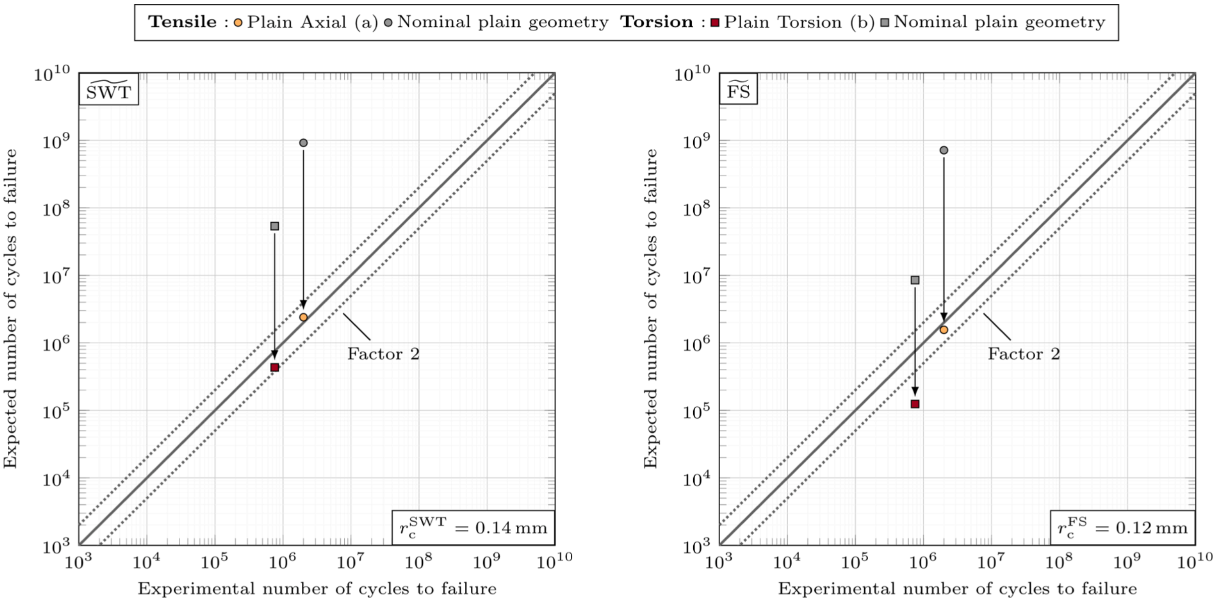

Fig. 11. Expected vs experimental number of cycles to failure obtained for porous plain specimens under fully reversed tensile and torsion loading by implementing $\widetilde{\text{SWT}}$ and $\widetilde{\text{FS}}$ CP factors.

be material within the process volume under consideration (e.g., thicknesses greater than the control radius). This can be easily monitored during the post-processing stage when applying the method on the finite element model, and it is particularly important in the case of complex geometries. Fig. 9c-d reports the ECP vs r_c curves in the case of torsion loading for both the $\widetilde{\text{SWT}}$ and $\widetilde{\text{FS}}$ cases; the curves show a slope change for a threshold value of the control radius of approximately 0.27 mm. In this case, the control volume intersects regions with other local CP maxima. Further investigations, which were not performed yet, would be necessary to verify whether this behavior could lead to invalidating the analysis. However, in the case of GJS600, the optimal control radii are significantly smaller than the threshold value, thus making the component fully analyzable. Such a situation does not occur in the case of Fig. 9a-b as the pore geometry presents a larger dimension with less intricate geometry compared to the torsion specimen.

After determining the maximum values of the $\widetilde{\text{SWT}}$ and $\widetilde{\text{FS}}$ factors for the examined pore specimens, the fatigue life prediction can be performed using data derived from experimental tests. Fig. 10 presents the predicted fatigue behavior of plain specimens with pores under tensile and torsional loads for the two ECP factors considered. The graphs additionally report the fatigue endurance curves obtained during the calibration phase. Fatigue predictions appear optimal for both loading conditions and for both ECP factors. Notably, the predictions would differ significantly if the pore geometry were not considered. For comparison, Fig. 10 includes the ECP model results for nominally plain specimens, which show a significant lower value of ECP factors.

Supporting this, Fig. 11 demonstrates that for both loading conditions, when $\widetilde{\mathrm{SWT}}$ is employed for fatigue prediction, the data points consistently fall within a scatter band of factor 2 solely by considering the correct pore geometry. In contrast, $\widetilde{\mathrm{FS}}$ provides a slightly less accurate prediction for the torsional specimen, with regard to the investigated material. This clearly highlights that considering only the nominal plain geometry, without modeling the pore, would lead to significant errors in fatigue life prediction.

5. Conclusions

This study explored the application of the Effective Critical Plane (ECP) approach for the fatigue assessment of ductile cast iron (DCI) components, particularly those with notches subjected to complex loading conditions. The ECP approach aims to enhance the accuracy of fatigue life predictions by integrating the critical plane hypothesis with the stress/strain averaging concept within a defined control volume. This study utilized the *Smith-Watson-Topper* (SWT) and *Fatemi-Socie* (FS) critical plane factors to illustrate the method's applicability. The following key conclusions can be drawn from this study:

1. the ECP method successfully provided accurate predictions of fatigue life for notched DCI components, demonstrating its robustness under various loading conditions and component geometries;
2. for the analyzed DCI material, the $\widetilde{\mathrm{SWT}}$ ECP factor showed a higher correlation with experimental fatigue data compared to the $\widetilde{\mathrm{FS}}$ parameter, an indication that the fatigue failure mechanism for the investigated material is better described by methods based on normal-rather than shear-based parameters;
3. the fatigue assessment employing linear elastic FE simulations and the $\widetilde{\mathrm{SWT}}$ ECP parameter yielded reliable fatigue life predictions for notched DCI specimens under both uniaxial, multiaxial, in-phase and out-of-phase loading conditions, with most results falling within a scatter band of factor 3;
4. the ECP method's reliance on a control radius r_c, which can be calibrated using two experimental fatigue curves, presents a significant advantage from an operational point of view; as a matter of fact, the calibration parameter r_c was obtained by means of two experimental fatigue curves of notched specimens tested under pure Mode I, which can be easily obtained through the use of resonant machines greatly speeding up fatigue testing;
5. the control radius value remained consistent across different mean stresses, notch severities, and fatigue lives, enhancing the method's applicability;
6. the method is computationally efficient and can be easily automated with finite element (FE) analysis, making it suitable for practical applications in engineering design (i.e. a few minutes of computation to solve the analysis of hundreds of thousands of nodes).

The integration of stress/strain averaging with critical plane methods presents significant advantages in fatigue assessment, particularly for materials like DCI, which are prone to casting defects such as micro-shrinkage porosity. By accurately predicting the fatigue life of notched components under complex loading conditions, the ECP method demonstrates substantial potential for real-world applications.

Future work will focus on further validation of the ECP method across a wider range of geometries, materials, and loading conditions. Additionally, the application of this methodology to real-world components will be explored to fully realize its potential in engineering design and fatigue life prediction.

CRediT authorship contribution statement

A. Chiocca: Writing – original draft, Visualization, Validation, Software, Methodology, Investigation, Data curation, Conceptualization. **M. Pedranz:** Writing – original draft, Validation, Methodology, Investigation, Data curation. **F. Zanini:** Writing – review & editing, Software, Investigation, Data curation. **S. Carmignato:** Writing – review & editing, Software, Investigation, Data curation. **V. Fontanari:** Writing – review & editing, Supervision, Resources, Project administration. **M. Benedetti:** Writing – review & editing, Supervision, Resources, Project administration. **F. Frendo:** Writing – review & editing, Supervision, Resources, Project administration, Methodology, Conceptualization.

Declaration of competing interest

The authors declare the following financial interests/personal relationships which may be considered as potential competing interests: [Andrea Chiocca reports financial support was provided by Government of Italy Ministry of Education University and Research.].

Acknowledgements

This paper is supported by the Italian Ministry of University and Research (MUR) as part of the PON 2014-2020 "Research and Innovation" resources – Green Action - DM MUR 1062/2021 - Title of the Research: *Sviluppo e riconversione di dispositivi automotive in ottica green: la decarbonizzazione dei veicoli e nuovi impieghi dei sistemi termo-idraulici*.

The present study received funding from Consiglio Nazionale delle Ricerche (CNR) and Fonderie Ariotti SpA in the form of a PhD grant for author Matteo Pedranz (doctorate school of *Innovazione Industriale* at the University of Trento).

Appendix A. Supplementary data

A Matlab script which implements the ECP $\widetilde{\mathrm{FS}}$ algorithm reported in the article has been uploaded to a GitHub repository: https://github.com/achiocca1/ECP. Supplementary data to this article can be found online at https://doi.org/10.5281/zenodo.14198237.

Data availability

Data will be made available on request.

References

[1] Bleicher C, Kaufmann H, Melz T. Assessment of service loads and material influence on the lifetime of thick-walled nodular cast iron components. Int J Fatigue 2021;147:106171. https://doi.org/10.1016/J.IJFATIGUE.2021.106171.

[2] Papadopoulos I. A comparative study of multiaxial high-cycle fatigue criteria for metals. Int J Fatigue 1997;19. https://doi.org/10.1016/S0142-1123(96)00064-3.

[3] Sines G, Ohgi G. Fatigue Criteria Under Combined Stresses or Strains. J Eng Mater Technol 1981;103. https://doi.org/10.1115/1.3224995.

[4] Kluger K, Łagoda T. New energy model for fatigue life determination under multiaxial loading with different mean values. Int J Fatigue 2014;66:229–45. https://doi.org/10.1016/J.IJFATIGUE.2014.04.008.

[5] Kluger K. Fatigue life estimation for 2017A–T4 and 6082–T6 aluminium alloys subjected to bending-torsion with mean stress. Int J Fatigue 2015;80:22–9. https://doi.org/10.1016/J.IJFATIGUE.2015.05.005.

[6] Zhang J, Xiao Q, Shi X, Fei B. Effect of mean shear stress on torsion fatigue failure behavior of 2A12-T4 aluminum alloy. Int J Fatigue 2014;67:173–82. https://doi.org/10.1016/J.IJFATIGUE.2013.11.012.

[7] Chen B, Carrion P, Grewal R, Inglis A, Hippman C, Morris E, et al. Short interpregnancy intervals, maternal folate levels, and infants born small for

gestational age: a preliminary study in a Canadian supplement-using population. Appl Physiol Nutr Metab 2017;42. https://doi.org/10.1139/apnm-2017-0292.

[8] Tovo R, Lazzarin P, Berto F, Cova M, Maggiolini E. Experimental investigation of the multiaxial fatigue strength of ductile cast iron. Theor Appl Fract Mech 2014;73:60–7. https://doi.org/10.1016/J.TAFMEC.2014.07.003.

[9] Wang XW, Shang DG, Sun YJ, Chen H. Multiaxial high-cycle fatigue life prediction model considering mean shear stress effect under constant and variable amplitude loading. Theor Appl Fract Mech 2018;96:676–87. https://doi.org/10.1016/J.TAFMEC.2017.10.007.

[10] McClaflin D, Fatemi A. Torsional deformation and fatigue of hardened steel including mean stress and stress gradient effects. Int J Fatigue 2004;26:773–84. https://doi.org/10.1016/J.IJFATIGUE.2003.10.019.

[11] Berto F, Lazzarin P, Yates JR. Multiaxial fatigue of V-notched steel specimens: A non-conventional application of the local energy method. Fatigue Fract Eng Mater Struct 2011;34:921–43. https://doi.org/10.1111/j.1460-2695.2011.01585.x.

[12] Tanaka K. Crack initiation and propagation in torsional fatigue of circumferentially notched steel bars. Int J Fatigue 2014;58:114–25. https://doi.org/10.1016/j.ijfatigue.2013.01.002.

[13] Benedetti M, Santus C, Raghavendra S, Lusuardi D, Zanini F, Carmignato S. Multiaxial plain and notch fatigue strength of thick-walled ductile cast iron EN-GJS-600-3: Combining multiaxial fatigue criteria, theory of critical distances, and defect sensitivity. Int J Fatigue 2022;156. https://doi.org/10.1016/j.ijfatigue.2021.106703.

[14] Berto F, Lazzarin P, Tovo R. Multiaxial fatigue strength of severely notched cast iron specimens. Int J Fatigue 2014;67. https://doi.org/10.1016/j.ijfatigue.2014.01.013.

[15] Carpinteri A, Spagnoli A, Vantadori S. Multiaxial fatigue assessment using a simplified critical plane-based criterion. Int J Fatigue 2011;33:969–76. https://doi.org/10.1016/J.IJFATIGUE.2011.01.004.

[16] Findley WN. A Theory for the Effect of Mean Stress on Fatigue of Metals Under Combined Torsion and Axial Load or Bending. Journal of Engineering for Industry 1959;81. https://doi.org/10.1115/1.4008327.

[17] Matake T. An Explanation on Fatigue Limit under Combined Stress. Bulletin of JSME 1977;20. https://doi.org/10.1299/jsme1958.20.257.

[18] Stanfield G. Discusson on "The strength of metals under combined alternating stresses." In: Gough H, Pollard H, editors. Proc. Inst. Mech. Eng. 131, 1935, p. 93.

[19] Brown MW, Miller KJ. A theory for fatigue failure under multiaxial stress-strain conditions. Proceedings of the Institution of Mechanical engineers 1973;187(1):745–55. https://doi.org/10.1243/PIME_PROC_1973_187_161_02.

[20] Commission of the European Communities. Joint Research Centre. Ispra Establishment., Metals Society., Associazione italiana di metallurgia., American Society for Metals. Mechanical behaviour and nuclear applications of stainless steel at elevated temperatures: proceedings of the international conference. Metals Society; 1982.

[21] J.L. R. Contribution à l'étude de la fatigue multi axiale sous sollicitations periodiques ou aléatoire. 1992.

[22] McDiarmid DL. A general criterion for high cycle multiaxial fatigue failure. Fatigue Fract Eng Mater Struct 1991;14. https://doi.org/10.1111/j.1460-2695.1991.tb00673.x.

[23] McDiarmid DL. A shear stress based critical-plane criterion of multiaxial fatigue failure for design and life prediction. Fatigue Fract Eng Mater Struct 1994;17. https://doi.org/10.1111/j.1460-2695.1994.tb00789.x.

[24] Wang CH, Brown MW. Life Prediction Techniques for Variable Amplitude Multiaxial Fatigue—Part 1: Theories. J Eng Mater Technol 1996;118. https://doi.org/10.1115/1.2806821.

[25] Fatemi A, Socie DF. A critical plane approach to multiaxial fatigue damage including out-of-phase loading. Fatigue Fract Eng Mater Struct 1988;11. https://doi.org/10.1111/j.1460-2695.1988.tb01169.x.

[26] Ince A, Glinka G. Innovative computational modeling of multiaxial fatigue analysis for notched components. Int J Fatigue 2016;82:134–45. https://doi.org/10.1016/J.IJFATIGUE.2015.03.019.

[27] Ince A, Glinka G. A generalized fatigue damage parameter for multiaxial fatigue life prediction under proportional and non-proportional loadings. Int J Fatigue 2014;62:34–41. https://doi.org/10.1016/J.IJFATIGUE.2013.10.007.

[28] Li D, Laurent A, Poncelet P. WebUser: mining unexpected web usage. International Journal of Business Intelligence and Data Mining 2011;6. https://doi.org/10.1504/IJBIDM.2011.038276.

[29] Liu J, Zhang Z, Li B, Lang S. Multiaxial fatigue life prediction of GH4169 alloy based on the critical plane method. Metals 2019;9(2):255. https://doi.org/10.3390/met9020255.

[30] Zhong B, Wang Y, Wei D, Wang J. A new life prediction model for multiaxial fatigue under proportional and non-proportional loading paths based on the pi-plane projection. Int J Fatigue 2017;102:241–51. https://doi.org/10.1016/J.IJFATIGUE.2017.04.013.

[31] Smith KN, Watson P, Topper TH. A Stress-Strain Function for the Fatigue of Metals. J Mater 1970;5:767–78.

[32] Socie D. Multiaxial Fatigue Damage Models. J Eng Mater Technol 1987;109:293–8. https://doi.org/10.1115/1.3225980.

[33] Gan L, Wu H, Zhong Z. Multiaxial fatigue life prediction based on a simplified energy-based model. Int J Fatigue 2021;144:106036. https://doi.org/10.1016/J.IJFATIGUE.2020.106036.

[34] Gates N, Fatemi A. Notch deformation and stress gradient effects in multiaxial fatigue. Theor Appl Fract Mech 2016;84:3–25. https://doi.org/10.1016/J.TAFMEC.2016.02.005.

[35] Zhao H, Liu J, Hua F, Ran Y, Zi R, Li B. Multiaxial fatigue life prediction model considering stress gradient and size effect. Int J Press Vessel Pip 2022;199:104703. https://doi.org/10.1016/J.IJPVP.2022.104703.

[36] Liu J, Zhao H, Ran Y, Hua F, Zi R. Multiaxial fatigue life prediction model with relative stress gradient and size effect. Fatigue Fract Eng Mater Struct 2022;45. https://doi.org/10.1111/ffe.13841.

[37] Neuber H. Kerbspannungslehre. Berlin Heidelberg: Springer; 1985.

[38] Berto F, Lazzarin P. Recent developments in brittle and quasi-brittle failure assessment of engineering materials by means of local approaches. Mater Sci Eng R Rep 2014;75. https://doi.org/10.1016/j.mser.2013.11.001.

[39] Taylor D. The Theory of Critical Distances, A New Perspective in Fracture Mechanics. 1st ed. Elsevier; 2007. https://doi.org/10.1016/B978-008044478-9/50002-8.

[40] Benedetti M, Santus C. Statistical properties of threshold and notch derived estimations of the critical distance according to the line method of the theory of critical distances. Int J Fatigue 2020;137. https://doi.org/10.1016/j.ijfatigue.2020.105656.

[41] Benedetti M, Santus C. Mean stress and plasticity effect prediction on notch fatigue and crack growth threshold, combining the theory of critical distances and multiaxial fatigue criteria. Fatigue Fract Eng Mater Struct 2019;42. https://doi.org/10.1111/ffe.12910.

[42] Santus C, Berto F, Pedranz M, Benedetti M. Mode III critical distance determination with optimized V-notched specimen under torsional fatigue and size effects on the inverse search probability distribution. Int J Fatigue 2021;151. https://doi.org/10.1016/j.ijfatigue.2021.106351.

[43] Santus C, Taylor D, Benedetti M. Experimental determination and sensitivity analysis of the fatigue critical distance obtained with rounded V-notched specimens. Int J Fatigue 2018;113. https://doi.org/10.1016/j.ijfatigue.2018.03.037.

[44] Santus C, Taylor D, Benedetti M. Determination of the fatigue critical distance according to the Line and the Point Methods with rounded V-notched specimen. Int J Fatigue 2018;106. https://doi.org/10.1016/j.ijfatigue.2017.10.002.

[45] Benedetti M, Santus C, Fontanari V, Lusuardi D, Zanini F, Carmignato S. Plain and notch fatigue strength of thick-walled ductile cast iron EN-GJS-600-3: A double-notch critical distance approach to defect sensitivity. Int J Fatigue 2021;152. https://doi.org/10.1016/j.ijfatigue.2021.106414.

[46] Berto F. A Brief Review of Some Local Approaches for the Failure Assessment of Brittle and Quasi-Brittle Materials. Adv Mater Sci Eng 2014; 2014.. https://doi.org/10.1155/2014/930679.

[47] Berto F, Lazzarin P. A review of the volume-based strain energy density approach applied to V-notches and welded structures. Theor Appl Fract Mech 2009;52. https://doi.org/10.1016/j.tafmec.2009.10.001.

[48] Pedranz M, Fontanari V, Santus C, Lusuardi D, Berto F, Benedetti M. A strain energy density design approach for large cast iron components: From microstructural analysis to multiaxial fatigue response. Int J Fatigue 2023;175:107824. https://doi.org/10.1016/j.ijfatigue.2023.107824.

[49] Pedranz M, Fontanari V, Raghavendra S, Santus C, Zanini F, Carmignato S, et al. A new energy based highly stressed volume concept to investigate the notch-pores interaction in thick-walled ductile cast iron subjected to uniaxial fatigue. Int J Fatigue 2023;169:107491. https://doi.org/10.1016/J.IJFATIGUE.2022.107491.

[50] Sgamma M, Chiocca A, Frendo F. Rapid and accurate semi-analytical method for the fatigue assessment with critical plane methods under non-proportional loading and material plasticity. Int J Fatigue 2024;182:108191. https://doi.org/10.1016/j.ijfatigue.2024.108191.

[51] Chiocca A, Frendo F, Marulo G. An efficient algorithm for critical plane factors evaluation. Int J Mech Sci 2023;242:107974. https://doi.org/10.1016/j.ijmecsci.2022.107974.

[52] Chiocca A, Sgamma M, Frendo F, Bucchi F. Rapid and accurate fatigue assessment by an efficient critical plane algorithm: application to a FSAE car rear upright. Procedia Struct Integrity 2023;47:749–56. https://doi.org/10.1016/j.prostr.2023.07.044.

[53] Chiocca A, Sgamma M, Frendo F, Bucchi F, Marulo G. Fatigue assessment of a FSAE car rear upright by a closed form solution of the critical plane method. Frattura Ed Integrità Strutturale 2023;18:153–62. https://doi.org/10.3221/IGF-ESIS.67.11.

[54] Chiocca A, Sgamma M, Frendo F. Closed-form solution for the *Fatemi-Socie* extended critical plane parameter in case of linear elasticity and proportional loading. Fatigue Fract Eng Mater Struct 2024;47:72–87. https://doi.org/10.1111/ffe.14153.

[55] Chiocca A, Frendo F. Fatigue assessment of structural components through the Effective Critical Plane factor. Int J Fatigue 2024;189:108565. https://doi.org/10.1016/j.ijfatigue.2024.108565.

[56] Chiocca A, Sgamma M, Frendo F. A closed-form solution for evaluating the Findley critical plane factor. Eur J Mech A Solids 2024;105:105274. https://doi.org/10.1016/j.euromechsol.2024.105274.

[57] Walat K, Kurek M, Ogonowski P, Łagoda T. The multiaxial random fatigue criteria based on strain and energy damage parameters on the critical plane for the low-cycle range. Int J Fatigue 2012;37:100–11. https://doi.org/10.1016/j.ijfatigue.2011.09.013.

[58] Kraft J, Linn A, Wächter M, Esderts A, Vormwald M. Multiaxial fatigue behavior and crack orientation prediction for steel and cast iron. Int J Fatigue 2024;183:108259. https://doi.org/10.1016/j.ijfatigue.2024.108259.